



Cite this: *Nanoscale*, 2024, **16**, 9781

## Catalytic $\text{NH}_3$ oxidation affected by the nanometric roughness of the platinum overlayer†

Masato Machida, <sup>a,b</sup> Nayu Yamasaki, <sup>c</sup> Tomoya Miyoshi, <sup>c</sup> Hiroki Kusaba, <sup>c</sup> Tetsuya Sato, <sup>d</sup> Keisuke Awaya, <sup>a</sup> Hiroshi Yoshida, <sup>a</sup> Junya Ohyama, <sup>a,b</sup> Teppei Ohori, <sup>e</sup> Kohei Oka, <sup>e</sup> Kenji Fujii<sup>e</sup> and Naoya Ishikawa<sup>e</sup>

Pulsed cathodic arc–plasma deposition was employed to create a few nanometre-thick Pt overlayer on a 50  $\mu\text{m}$ -thick Fe–Cr–Al metal (SUS) foil, resulting in an effective  $\text{NH}_3$  oxidation catalyst fabrication. This catalyst exhibited a turnover frequency (TOF) exceeding 100 times that of Pt nanoparticles. In this study, Pt overlayer catalysts with varying degrees of surface roughness were fabricated using different metal foil substrates: mirror-polished (Pt/p-SUS), unpolished (Pt/SUS) and roughened by the formation of a surface oxide layer (Pt/ $\text{Al}_2\text{O}_3$ /SUS). The nanoscale roughness was comprehensively analysed using electron microscopy, laser scanning confocal microscopy and chemisorption techniques.  $\text{NH}_3$  oxidation activity, measured at 200 °C, followed an increasing trend in the order of Pt/ $\text{Al}_2\text{O}_3$ /SUS < Pt/SUS < Pt/p-SUS, despite a decrease in the apparent Pt surface area in the same order. Consequently, the calculated TOF was markedly higher for Pt/p-SUS (267  $\text{min}^{-1}$ ) compared to Pt/SUS (107  $\text{min}^{-1}$ ) and Pt/ $\text{Al}_2\text{O}_3$ /SUS ( $\leq 22 \text{ min}^{-1}$ ). The smooth Pt overlayer surface also favoured  $\text{N}_2$  yield over  $\text{N}_2\text{O}$  at this temperature. This discovery enhances our fundamental understanding of high-TOF  $\text{NH}_3$  oxidation over Pt overlayer catalysts, which holds significance for the advancement and industrial implementation of selective  $\text{NH}_3$  oxidation processes.

Received 17th March 2024,  
Accepted 28th April 2024

DOI: 10.1039/d4nr01156b  
[rsc.li/nanoscale](http://rsc.li/nanoscale)

### 1. Introduction

Currently, many practical solid catalysts are engineered to produce active metal nanoparticles dispersed on porous support materials boasting large specific surface areas. In simple terms, this aims to amplify the number of active sites per unit mass, thereby achieving high reaction rates. Another strategy for enhancing catalytic performance involves boosting intrinsic activity, quantified in terms of turnover frequency (TOF). Because TOF denotes the molar number of reactant molecules reacted by one mole of catalyst active sites per unit time, and consequently, the apparent catalytic activity corre-

ponds to TOF multiplied by the number of active sites, an increase in TOF leads to increased reaction rates. However, currently, no systematic and comprehensive methodology is in place to precisely control the TOF of each catalyst.

Recently, our research unveiled the remarkable efficacy of nanometre-thick precious metal overlayers that entirely cover inert metal foil substrates in achieving exceptionally high TOF for specific chemical reactions compared to their nanoparticle counterparts.<sup>1–8</sup> For instance, a few-nanometre-thick Rh overlayer demonstrated TOF exceeding that of Rh nanoparticles by two orders of magnitude, particularly notable in the NO with CO reaction crucial for automotive three-way catalysis (TWC).<sup>1,2</sup> Another illustrative example is the catalytic  $\text{NH}_3$  oxidation essential for  $\text{NH}_3$  slip catalysis (ASC).<sup>9–12</sup> It is widely acknowledged that Pt is among the most active catalysts, especially at low temperatures ( $\leq 200$  °C) in the presence of water vapour ( $\sim 10$  vol%).<sup>13–21</sup> A few-nanometre-thick Pt overlayer on the metal foil substrate exhibited  $\text{NH}_3$  oxidation activity comparable to or even superior to Pt nanoparticle catalysts like Pt/ $\gamma\text{-Al}_2\text{O}_3$ .<sup>4</sup> This increased  $\text{NH}_3$  oxidation rate was facilitated by the exceedingly high TOF of the Pt overlayer, approximately 180 times greater than that achieved with Pt/ $\gamma\text{-Al}_2\text{O}_3$  at 200 °C. Similar observations of high-TOF  $\text{NH}_3$  oxidation were noted for Ir overlayer catalysts.<sup>5</sup> Notably, when these metal foil catalysts were shaped into honeycomb

<sup>a</sup>Division of Materials Science and Chemistry, Faculty of Advanced Science and Technology, Kumamoto University, 2-39-1 Kurokami, Chuo, Kumamoto 860-8555, Japan. E-mail: [machida@kumamoto-u.ac.jp](mailto:machida@kumamoto-u.ac.jp); Fax: +81-96-342-3651

<sup>b</sup>Institute of Industrial Nanomaterials, Kumamoto University, 2-39-1 Kurokami, Chuo, Kumamoto 860-8555, Japan

<sup>c</sup>Department of Applied Chemistry and Biochemistry, Graduate School of Science and Technology, Kumamoto University, 2-39-1 Kurokami, Chuo, Kumamoto, 860-8555, Japan

<sup>d</sup>Technical Division, Kumamoto University, 2-39-1 Kurokami, Chuo, Kumamoto, 860-8555, Japan

<sup>e</sup>Isuzu Advanced Engineering Center, Ltd, 8 Tsuchidana, Fujisawa, 252-0881, Japan  
† Electronic supplementary information (ESI) available. See DOI: <https://doi.org/10.1039/d4nr01156b>

configurations, they achieved performances comparable to conventional washcoated ceramic honeycomb catalysts containing metal nanoparticles under practical conditions (GHSV  $> 10^5 \text{ h}^{-1}$ ) for both TWC and ASC. Moreover, these innovative honeycomb catalysts with metal overlayer structures utilise fewer precious metals than conventional nanoparticle catalysts. This advancement will be widely recognised as a future research trajectory owing to the limited supply and increasing demand for precious metals in various other applications. Design of novel honeycomb catalysts based on metal overlayers and/or metal foils has also been proposed by several research groups.<sup>22–24</sup>

From a fundamental viewpoint, the high TOFs observed over metal overlayer catalysts resemble particle size-dependent reactivity changes, *i.e.*, increased TOF with increasing metal particle size, a phenomenon known as structure-sensitive catalytic reaction.<sup>25–27</sup> For example, the superior performance of the Rh overlayer over nanoparticles is evident in the structure-sensitive CO–NO reaction but not in the structure-insensitive CO–O<sub>2</sub> reaction.<sup>2</sup> Conversely, while the Rh overlayer exhibits high TOF in the CO–NO reaction, the same cannot be said for the Pd overlayer.<sup>2</sup> Thus, the feasibility of achieving high TOF with metal overlayers is strongly dependent on the specific metal elements and catalytic reactions employed. Through experimental and theoretical studies, we have discovered distinct energy barriers for NO dissociation followed by N–N recombination. Notably, the N–N recombination on the Rh (111) overlayer surface occurs faster than on the Rh nanoparticles (Rh<sub>55</sub> cluster), suggesting that this reduced energy barrier directly enhances the TOF of the Rh overlayer in the CO–NO reaction.<sup>2</sup>

It is also established that Pt catalysts with larger particle sizes demonstrate greater TOF than those with smaller particle sizes. This phenomenon has been observed across various oxidation reactions involving NH<sub>3</sub>,<sup>28–30</sup> NO<sup>31</sup> and various hydrocarbons,<sup>32–35</sup> where the binding energy of adsorbed oxygen on Pt metal surfaces tends to decrease with increasing particle size. Furthermore, as the Pt particle size increases, the oxidation state of the Pt surface tends to shift from oxidic to metallic.<sup>36,37</sup> The high TOF observed in the NH<sub>3</sub> oxidation of the Pt overlayer in our previous study was attributed to the increased resistance of metallic Pt species against oxidation in excess O<sub>2</sub>, compared to Pt nanoparticles, which are prone to oxidation into less active Pt oxide.<sup>4</sup> Considering the surface sensitivity of catalytic reactions, closely tied to the nanostructure of exposed surfaces (terrace, corner and/or edge sites), the surface roughness of metal overlayers could influence TOF and thus affect apparent catalytic performance. However, there is insufficient understanding of how surface roughness impacts the TOFs of metal overlayer catalysts.

In this study, we investigated the correlation between the nanometric surface roughness of a Pt metal overlayer and its TOFs for catalytic NH<sub>3</sub> oxidation. We found that TOF was indeed sensitive to the nanoscale surface roughness of Pt overlayer catalysts when the metal foil substrate was either mirror-polished or roughened by forming a surface oxide layer *via*

heat treatment before the arc-plasma (AP) deposition of Pt. Consequently, the surface nanostructures of the as-prepared Pt overlayer catalysts were analysed using X-ray diffraction (XRD), X-ray photoelectron spectroscopy (XPS), electron microscopy and laser scanning confocal microscopy. Based on these results, we obtained valuable insights to aid in the rational design of this innovative nanocatalyst system employing a two-dimensional metal surface.

## 2. Experimental section

### 2.1. Preparation of Pt overlayer catalysts

The Pt overlayer catalysts were fabricated through pulsed cathodic AP deposition of Pt onto a flat and thin Fe–Cr–Al foil (75 mass% Fe, 20 mass% Cr and 5 mass% Al, 50  $\mu\text{m}$ -thick, JFE20-5USR, JFE Steel, Japan) serving as a substrate. The metal foil, referred to as SUS, was utilised as received, subjected to mirror polishing, or underwent thermal treatment. Mirror polishing of the metal foil was achieved using a Buehler MetaServ 250 grinder-polisher employing a diamond suspension solution with particle sizes ranging between 1 and 3  $\mu\text{m}$ . Subsequently, a 0.05  $\mu\text{m}$  Al<sub>2</sub>O<sub>3</sub> polishing paste was applied until the surface roughness ( $R_a$ ) reached less than 10 nm. XPS analysis indicated that no contamination elements were detected on the surface of polished metal foils. Thermal treatment of the as-supplied metal foil was conducted under air at 900 °C for 20 h to form a surface Al oxide layer. The mirror-polished and thermally treated metal foils were denoted as p-SUS and Al<sub>2</sub>O<sub>3</sub>/SUS, respectively. The AP deposition of Pt onto these metal foils, each measuring 30 mm  $\times$  30 mm, was carried out under vacuum conditions ( $< 10^{-3}$  Pa) at ambient temperature, following protocols established in our previous studies (Fig. S1†).<sup>4–6</sup> The experimental setup comprised a vacuum chamber, a turbo-molecular pumping system and an arc discharge source (ARL-300, Ulvac, Japan). A tubular Pt metal (10 mm in outer diameter, 7 mm in inner diameter and 17 mm in length, 99.9%, Furuya Metals, Japan) served as a cathodic target, generating 2000 shots of AP pulses with a period of 0.2 ms and a frequency of 1 Hz to irradiate the foil. Unless specified otherwise, this is the standard condition for preparing the Pt overlayer, while the number of AP pulses was increased to 8000 shots for structural characterisation purposes, as described below. The mass of the as-deposited Pt was monitored *in situ* using a quartz crystal microbalance (STM-2, Inficon, Switzerland).

### 2.2. Characterisation

XRD measurements of the Pt overlayer catalysts were conducted using a Rigaku RINT-TTR III diffractometer with monochromatic Cu K $\alpha$  radiation (40 kV and 200 mA) operating in a symmetric 2 $\theta$ – $\theta$  scan mode. The surface topography of the foil, with and without a surface oxide layer, was analysed using 3D laser scanning confocal microscopy (VK-X3000, Keyence). XPS spectra were acquired using a Thermo Scientific K-Alpha instrument with monochromatic Al K $\alpha$  radiation (1486.6 eV).

The C 1s binding energy of 285 eV was utilised as a reference to correct for surface charge effects. The surface structure of the film catalysts was examined using Hitachi S-4800 and JEOL JSM-7800F scanning electron microscopy (SEM) instruments operated at 10 kV accelerating voltage. For scanning transmission electron microscopy (STEM) analysis, a cross-sectional specimen of the film catalyst was prepared using a focused ion beam (FIB) system (XVision 200TB, SII NanoTechnology) employing a  $\text{Ga}^+$  ion beam. High-angle annular dark-field (HAADF), high-resolution transmission electron microscopy and X-ray mapping images of a cross-sectioned thin film catalyst were analysed using a Talos F200X (Thermo Scientific) apparatus under 200 kV acceleration voltage, equipped with an energy-dispersive spectrometer (EDS) for elemental analysis. The Pt surface area was determined *via* pulsed CO chemisorption technique at 50 °C (Belcat, Bel Japan) following treatment under an  $\text{H}_2$  flow (200 °C, 30 min). This method was applied only to the  $\text{Pt}/\text{Al}_2\text{O}_3/\text{SUS}$  sample because the other samples exhibited negligible adsorption owing to their extremely small Pt surface areas.

### 2.3. Catalytic reactions

The catalytic test for  $\text{NH}_3$  oxidation was conducted at atmospheric pressure using a strip-shaped foil catalyst ( $3 \times 30 \text{ mm}^2$ ), with one side coated with a Pt layer (2000-shot AP pulses). The detailed experimental setup of the conventional flow reactor is illustrated in Fig. S2.†  $\text{NH}_3$  oxidation activity was assessed under steady-state conditions. The catalyst bed was incrementally heated from 100 °C to 300 °C while supplied with a simulated gas mixture comprising 300 ppm  $\text{NH}_3$ , 8%  $\text{O}_2$ , 10%  $\text{H}_2\text{O}$  and a He balance at a flow rate of 100  $\text{mL min}^{-1}$ . Concentrations of  $\text{NH}_3$ ,  $\text{NO}$ ,  $\text{N}_2\text{O}$  and  $\text{NO}_2$  were monitored using an online Fourier-transform infrared spectrometer (Nicolet iS50, Thermo Fisher Scientific, USA) equipped with a temperature-controllable gas cell (2 m optical path length) maintained at 120 °C. The  $\text{N}_2$  concentration downstream of the catalyst bed was estimated by subtracting the total concentration of analysed gas species ( $\text{NH}_3$ ,  $\text{NO}$ ,  $\text{N}_2\text{O}$ , and  $\text{NO}_2$ ) from the initial  $\text{NH}_3$  concentration (300 ppm).

## 3. Results and discussion

### 3.1. Structure of Pt overlayer catalysts

The XRD patterns of the metal foil catalysts are depicted in Fig. 1. Here, the Pt overlayer was prepared using 8000-shot AP pulses to ensure the adequate intensity of X-ray reflection. The Pt overlayer formed on a mirror-polished SUS foil (Pt/p-SUS) and an unpolished SUS foil (Pt/SUS) exhibited peaks corresponding to the face-centred cubic Pt and those attributed to the body-centred cubic Fe–Cr–Al alloy. As previously reported,<sup>4</sup> the as-prepared Pt overlayer displayed the (111) orientation because the (111) plane of a face-centred cubic Pt lattice offers the lowest surface energy among low-index planes. This was evident for the Pt/p-SUS sample, with a relative intensity ratio of  $I_{111}:I_{200}:I_{220} = 100:18:4$ , compared to a polycrystalline Pt

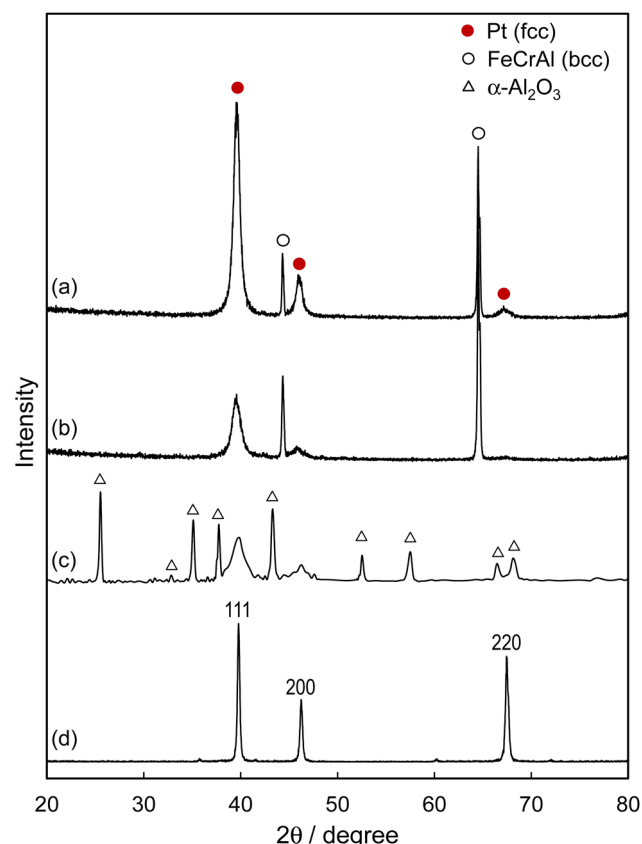


**Fig. 1** XRD patterns of film catalysts on SUS (Fe–Cr–Al) foil. (a)  $\text{Pt}/\text{p-SUS}$ , (b)  $\text{Pt}/\text{SUS}$ , (c)  $\text{Pt}/\text{Al}_2\text{O}_3/\text{SUS}$  and (d) polycrystalline Pt plate. To enhance reflection intensity, Pt was coated onto SUS foils using 8000-shot AP pulses.

plate ( $I_{111}:I_{200}:I_{220} = 100:46:80$ ). The Pt overlayer formed on the thermally treated SUS foil ( $\text{Pt}/\text{Al}_2\text{O}_3/\text{SUS}$ ) exhibited a highly crystalline  $\alpha\text{-Al}_2\text{O}_3$  layer covering the surface of the metal foil, indicating that the aluminium within the Fe–Cr–Al foil underwent oxidation to form a surface passivation layer. The diffraction peaks attributed to Pt showed no preferential orientation, with a relative intensity ratio of  $I_{111}:I_{200}$  resembling that of the polycrystalline Pt plate (100:46). The absence of preferential orientation in the Pt overlayer is linked to its structural characteristics, as discussed below.

The XPS analysis of the Pt/p-SUS and Pt/SUS samples (Fig. S3†) revealed complete coverage of the SUS surfaces by Pt overlayers despite the different surface roughness described below. The amount of deposited Pt was estimated to be approximately 2 nm thick (using 2000-shot AP pulses), assuming deposition onto a completely flat surface. Upon treatment of the SUS foil in the air at 900 °C for 20 h, the Al and O peaks exhibited significant intensification, while the other metal peaks (Fe and Cr) disappeared. Following subsequent AP deposition of Pt, all Al peaks disappeared, concomitant with the appearance of Pt peaks, indicating almost complete surface coverage by Pt regardless of the presence of an Al oxide layer on the foil surface ( $\text{Pt}/\text{Al}_2\text{O}_3/\text{SUS}$ ). Thus, complete surface cov-

erage by the Pt overlayer was achieved for all these metal foil catalysts.

Fig. 2 presents SEM images illustrating the surface characteristics of these metal foil catalysts. The mirror-polished Pt/p-SUS sample (a) displayed a notably smooth surface compared to the unpolished Pt/SUS sample (b). Conversely, Pt/Al<sub>2</sub>O<sub>3</sub>/SUS (c) exhibited a significantly higher degree of surface roughness owing to the rod-like texture of  $\alpha$ -Al<sub>2</sub>O<sub>3</sub> deposits, measuring approximately 0.2  $\mu\text{m}$  thick and 0.5–1  $\mu\text{m}$  long. The texture of the Pt overlayer was not discernible in the SEM images owing to its small size, falling below the resolution limit. Quantitative surface roughness analyses were conducted using a 3D laser scanning confocal microscope, as depicted at the bottom of Fig. 2. Compared to the polished Pt/p-SUS sample (a) with an average surface roughness ( $R_a$ ) of only 8 nm, the Pt/SUS sample (b) exhibited a larger  $R_a$  of approximately 94 nm owing to contoured deformation texture formed during the manufacturing rolling process of the SUS foil. On the Pt/Al<sub>2</sub>O<sub>3</sub>/SUS sample (c), the  $R_a$  value significantly increased to 179 nm. The surface area ratio (Sdr), defined as the increment of the total surface area relative to the flat sampling area (213  $\times$  300  $\mu\text{m}$ ), was determined through topographic analysis. The Sdr increased from 0.0001 (a) to 0.011 (b), then to 0.607 (c), indicating an active Pt surface area ratio of 1.000 : 1.011 : 1.607. Consequently, the roughness of the surface Al<sub>2</sub>O<sub>3</sub> layer formed by heat treatment in the air (c) is inferred to provide a larger number of active sites than the extremely smooth surface of Pt/p-SUS (a).

The surface topographic analysis highlighted the Pt overlayer's contrasting roughness between the Pt/p-SUS and Pt/Al<sub>2</sub>O<sub>3</sub>/SUS samples. For a more comprehensive structural assessment of these Pt overlayer catalysts, the cross-sectional view near the surface of the Pt overlayer was examined through STEM and X-ray mapping analyses. In the case of the Pt/p-SUS sample, the thickness of the Pt overlayer was increased (using 8000-shot AP pulses) to enhance visibility. As depicted in Fig. 3a, Pt/p-SUS exhibited an exceptionally flat and smooth surface with nanometre-level precision. The Pt overlayer displayed continuous growth along the SUS surface, establishing intimate contact. An enlarged image (Fig. 3b) and X-ray mapping images (Fig. 3c) revealed the absence of grain boundaries in the 6 nm-thick Pt overlayer. However, the Pt and SUS foil detected a 2 nm-thick corrosion layer containing Al, Cr and O. This layer likely formed during the mirror polishing process before the AP deposition of Pt overlayers. The Pt overlayer exhibited intimate contact with the corrosion layer, with a clear interface devoid of diffusion of each constituent atom.

The cross-sectional images of the Pt overlayer structure formed on the Al<sub>2</sub>O<sub>3</sub>/SUS foil are depicted in Fig. 4. In stark contrast to Pt/p-SUS (Fig. 3), the surface of Pt/Al<sub>2</sub>O<sub>3</sub>/SUS exhibited significant roughness and undulations. The inner  $\alpha$ -Al<sub>2</sub>O<sub>3</sub> layer in contact with the metal foil had a thickness of approximately 1.0–1.4  $\mu\text{m}$  and a surface roughness of a few hundred nanometres (Fig. 4a). X-ray elemental mapping analysis revealed that this layer contained Al and O but not Fe and Cr (Fig. S4†), consistent with forming a dense and adherent

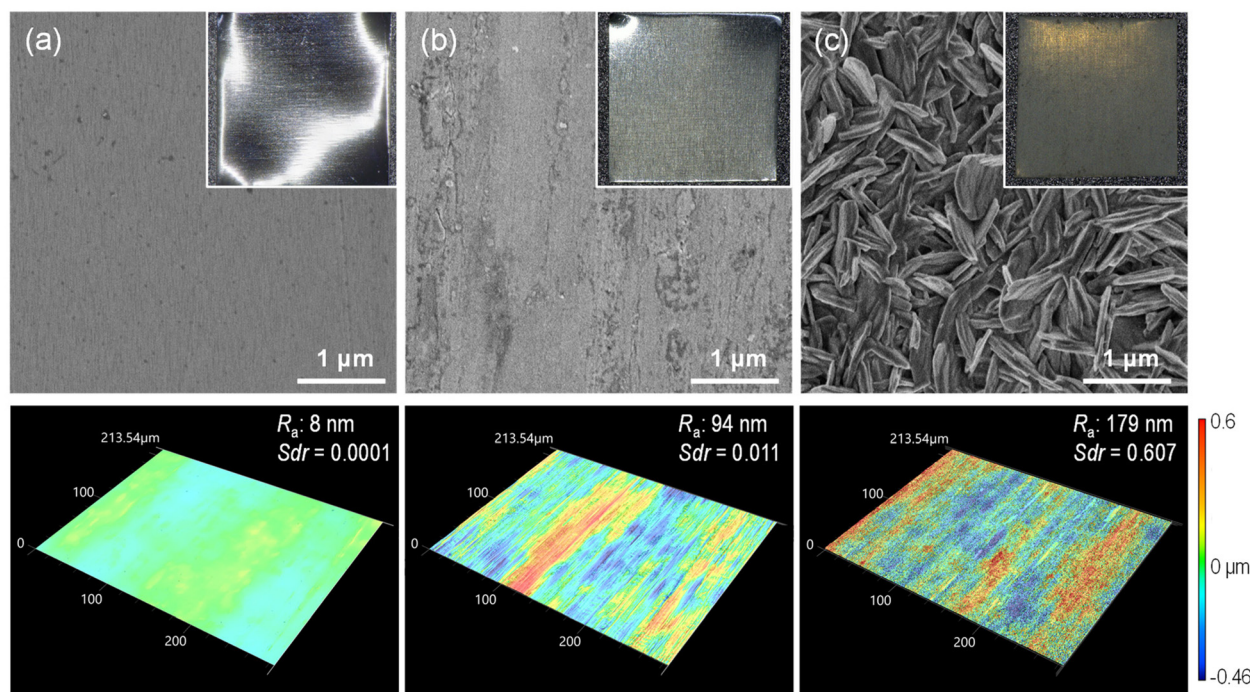


**Fig. 2** SEM and 3D laser scanning confocal microscope images of the surfaces of (a) Pt/p-SUS, (b) Pt/SUS, and (c) Pt/Al<sub>2</sub>O<sub>3</sub>/SUS. Insets in the upper images depict the overall foil samples sized 30  $\times$  30  $\mu\text{m}^2$ .  $R_a$  and Sdr values (insets of the bottom images) denote surface roughness and surface area ratio, respectively. Pt was deposited onto SUS foils using 2000-shot AP pulses.

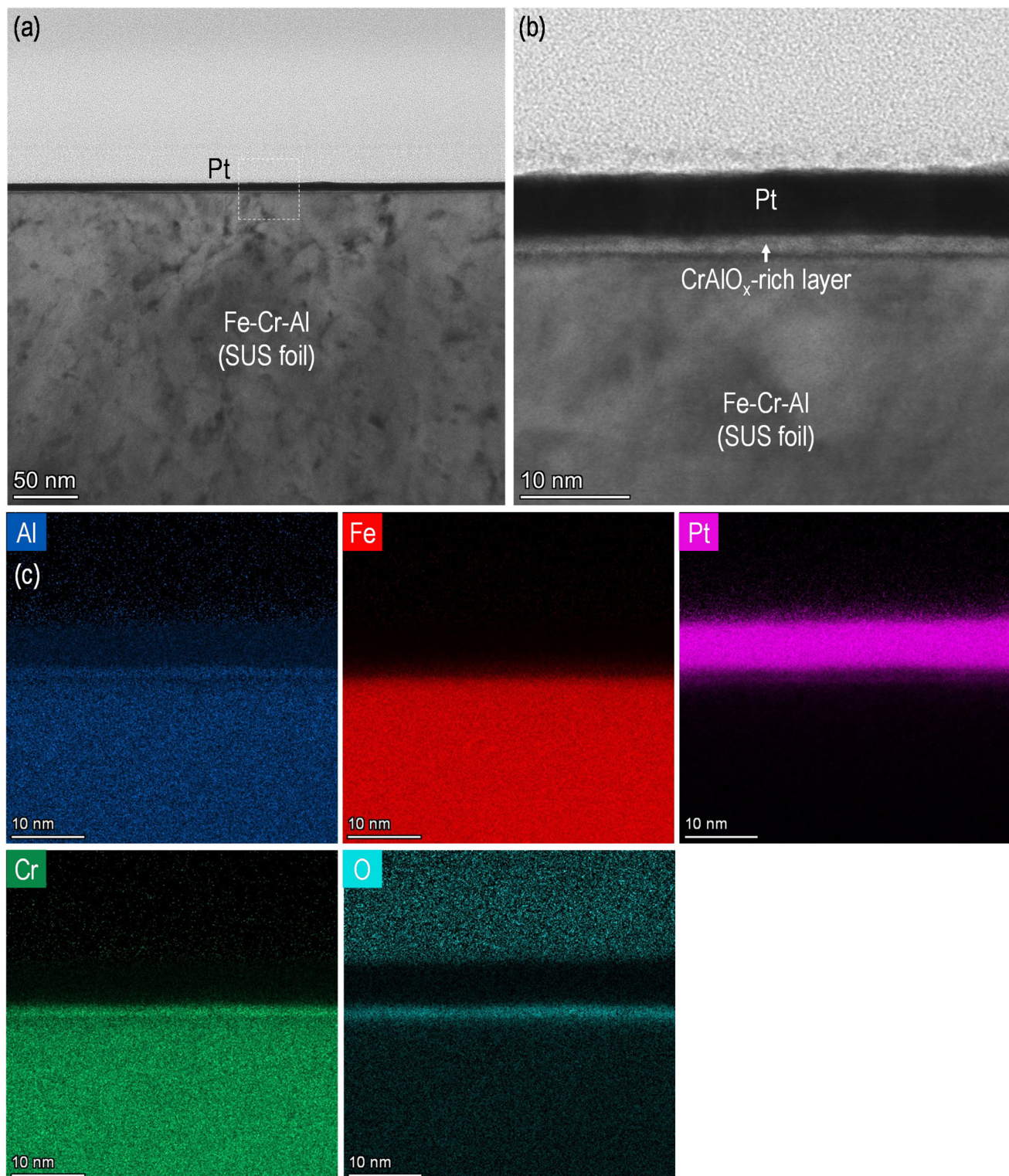


**Fig. 3** (a) STEM image of the cross-sectional Pt overlayer structure formed on the p-SUS foil. (b) An enlarged image was obtained from a dashed square region of (a). (c) X-ray images obtained from a square region of (a). Pt was deposited onto the SUS foil using 8000-shot AP pulses to enhance visibility.

$\alpha$ -Al<sub>2</sub>O<sub>3</sub> layer during thermal treatment at 900 °C in air. This surface passivation layer protects the metal foil from further oxidation, ensuring high-temperature stability.<sup>38</sup> The dashed

square region in the upper right part of Fig. 4a was magnified and analysed by EDS (Fig. 4b-d). The outermost surface of the Al<sub>2</sub>O<sub>3</sub> layer was entirely covered by a layer of Pt nanoparticles a

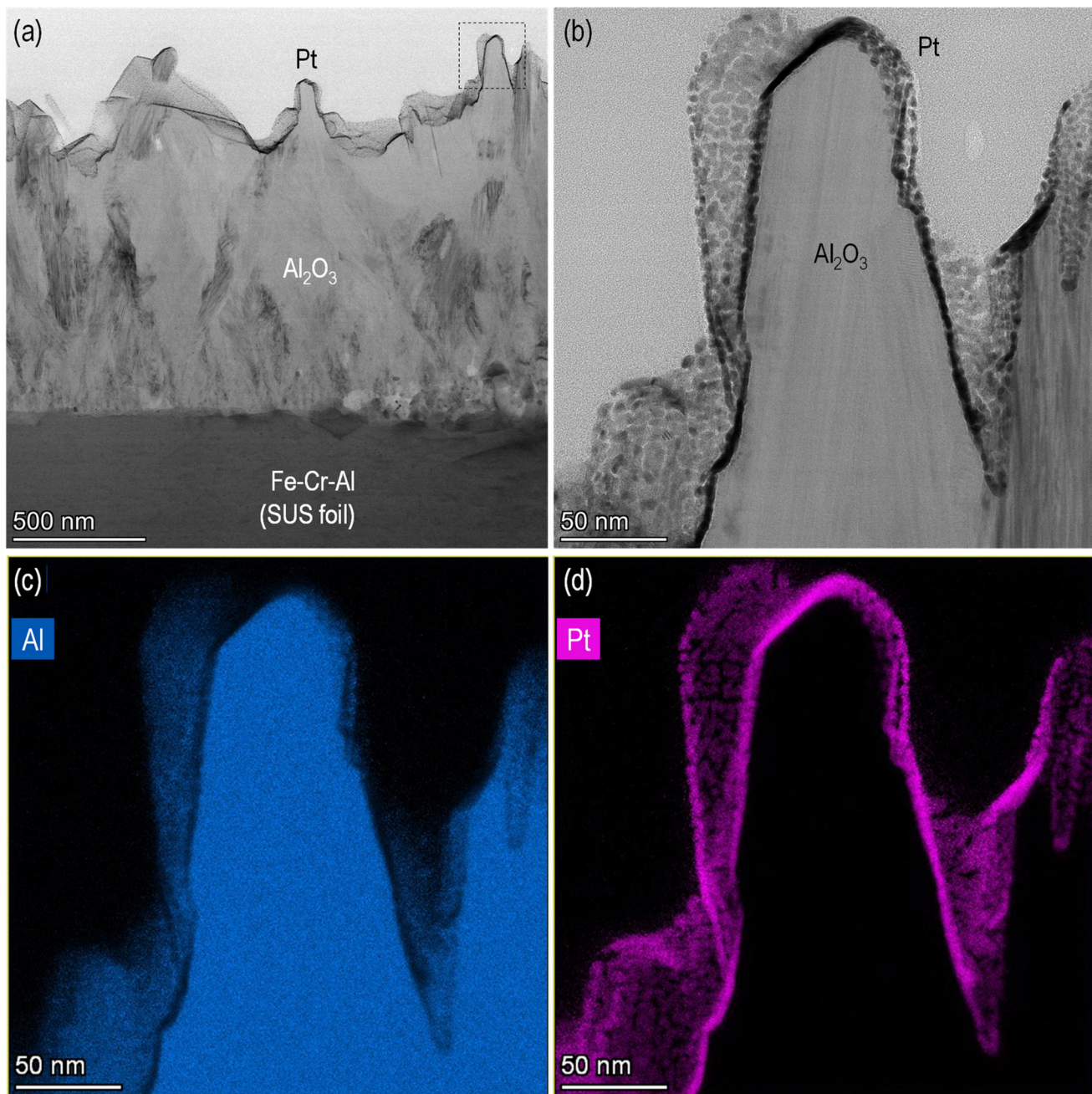


**Fig. 4** (a) STEM image of the cross-sectional Pt overlayer structure formed on the  $\text{Al}_2\text{O}_3$ /SUS foil. (b) An enlarged image was obtained from a dashed square region of (a). (c) Al and (d) Pt X-ray images obtained from a square region of (a). Pt was deposited onto the  $\text{Al}_2\text{O}_3$ /SUS foil using 8000-shot AP pulses to enhance visibility.

few nanometres thick, formed by pulsed AP deposition, in agreement with the XPS analysis results as described earlier. Notably, the Pt overlayer did not form a continuous coating film but exhibited a stone-wall-like nanotexture comprising closely packed nanometre-sized Pt particles. The overlayer structure displayed no gap beneath the Pt layer, ensuring intimate and strong contact with the  $\text{Al}_2\text{O}_3$  layer. The stone-wall structure, arising from the surface roughness of the  $\text{Al}_2\text{O}_3$  layer, provided a larger Pt surface area compared to Pt/p-SUS,

as illustrated in Fig. 2, thereby enhancing catalytic performance. However, interestingly, this expectation was not fully realised, as detailed in the following section.

### 3.2. Catalytic $\text{NH}_3$ oxidation and turnover frequency (TOF)

Catalytic  $\text{NH}_3$  oxidation was performed using strips ( $3 \times 30 \text{ mm}^2$ ) of the as-prepared Pt/p-SUS, Pt/SUS, and Pt/ $\text{Al}_2\text{O}_3$ /SUS samples. When subjected to 2000-shot AP pulsed irradiation on one side only, all three samples received the same amount

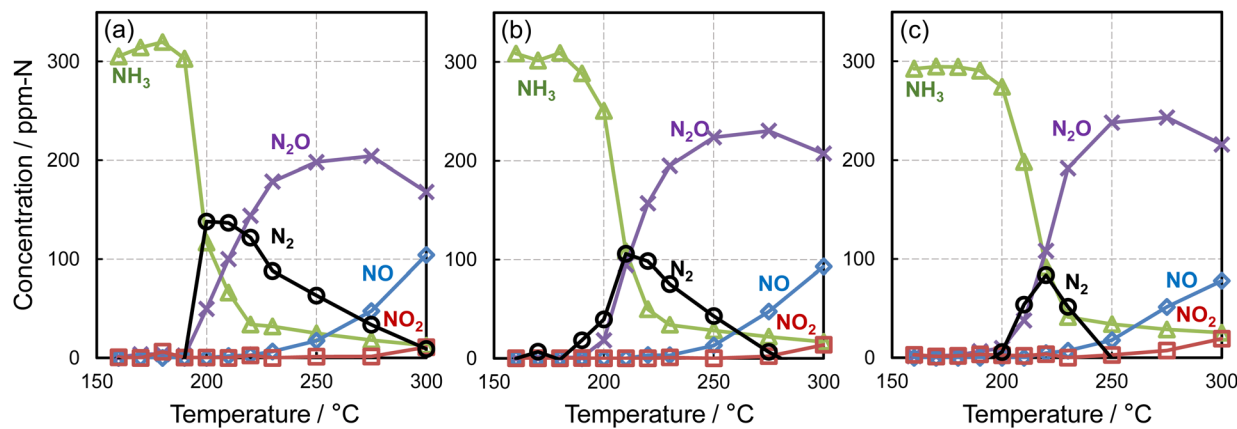


Fig. 5 Temperature dependence of  $\text{NH}_3$  oxidation and product selectivity over a strip ( $3 \times 30 \text{ mm}^2$ ) of (a) Pt/p-SUS, (b) Pt/SUS and (c) Pt/ $\text{Al}_2\text{O}_3$ /SUS. Pt was deposited using 2000-shot AP pulses on one side of SUS foils. Gas feed composition: 300 ppm  $\text{NH}_3$ , 8%  $\text{O}_2$ , 10%  $\text{H}_2\text{O}$ , and He balance,  $100 \text{ mL min}^{-1}$ .

of Pt deposition. However, their Pt surface areas differed based on surface roughness, increasing in the following order: Pt/p-SUS < Pt/SUS < Pt/ $\text{Al}_2\text{O}_3$ /SUS, as evidenced by surface topographic analysis (Fig. 2). The temperature dependency of  $\text{NH}_3$  conversion and product yields is illustrated in Fig. 5. All catalysts exhibited a sharp decline in  $\text{NH}_3$  concentration starting at temperatures  $\geq 200^\circ\text{C}$ , accompanied by the formation of  $\text{N}_2\text{O}$  and  $\text{N}_2$ . Subsequently, with further temperature increase,  $\text{N}_2\text{O}/\text{N}_2$  formation tended to decrease, while the formation of  $\text{NO}/\text{NO}_2$  commenced at temperatures  $\geq 250^\circ\text{C}$ . Particularly noteworthy was the significant difference in catalytic activity at the lowest temperature near  $200^\circ\text{C}$ , where the Pt/p-SUS sample (Fig. 5a) demonstrated notably higher  $\text{NH}_3$  conversion and  $\text{N}_2$  yield values despite having the smallest Pt surface area owing to its smooth surface. Conversely, Pt/SUS and Pt/ $\text{Al}_2\text{O}_3$ /SUS exhibited lower activities at this temperature (b, c).

The TOF for  $\text{NH}_3$  conversion at  $200^\circ\text{C}$  was calculated (Table 1). Owing to the exceptionally high  $\text{NH}_3$  conversion over Pt/p-SUS ( $>60\%$ , Fig. 5a) at  $200^\circ\text{C}$ , a smaller strip size ( $3 \times 10 \text{ mm}^2$ ) was utilised to determine TOF. The number of surface Pt sites was calculated using the geometric area of the foils, Pt surface coverage, Sdr and the surface atomic density of Pt. For Pt/ $\text{Al}_2\text{O}_3$ /SUS, the surface Pt site was also quantified using the amount of CO uptake. Details of the TOF calculation are outlined in Table S1.† As displayed in Table 1, TOF exhibi-

ted a significant increase in the order Pt/ $\text{Al}_2\text{O}_3$ /SUS < Pt/SUS < Pt/p-SUS, contrary to the order of the Pt surface area described earlier. TOF for Pt/p-SUS ( $267 \text{ min}^{-1}$ ) surpassed that of Pt/SUS ( $107 \text{ min}^{-1}$ ) by over 2-fold and exceeded that of Pt/ $\text{Al}_2\text{O}_3$ /SUS ( $\leq 22 \text{ min}^{-1}$ ) by more than 10-fold. Hence, the smoothest Pt overlayer achieved the highest TOF for  $\text{NH}_3$  oxidation, indicating a negative effect of Pt overlayer roughness on TOF. Previously, our study reported a TOF of approximately  $52 \text{ min}^{-1}$  for Pt/SUS, which was over 180-fold greater than that of the reference Pt/ $\text{Al}_2\text{O}_3$  powder catalyst ( $0.28 \text{ min}^{-1}$ ) containing Pt nanoparticles with an average size of approximately 3 nm.<sup>4</sup> Consequently, the Pt/ $\text{Al}_2\text{O}_3$ /SUS in this study displayed an intermediate TOF value between those of Pt/SUS and Pt/ $\text{Al}_2\text{O}_3$ . As depicted in Fig. 5,  $\text{NH}_3$  conversions and product yields over the three metal foil catalysts were nearly comparable at temperatures equal to or higher than  $225^\circ\text{C}$ . On Pt/p-SUS,  $\text{N}_2$  predominantly formed at  $200^\circ\text{C}$  but gradually decreased with increasing temperature. Conversely, Pt/SUS and Pt/ $\text{Al}_2\text{O}_3$ /SUS exhibited a steeper decline in  $\text{N}_2$  yield at elevated temperatures. Thus, the smooth Pt overlayer appears beneficial for accelerating  $\text{NH}_3$  oxidation and enhancing  $\text{N}_2$  selectivity.

Pt/p-SUS exhibited a notably higher TOF than Pt/SUS and Pt/ $\text{Al}_2\text{O}_3$ /SUS. The underlying reason for this discrepancy in TOF remains unclear; however, this ranking aligns with the order of surface roughness depicted in Fig. 2. To obtain more

Table 1 Activity comparison between Pt/p-SUS, Pt/SUS, and Pt/ $\text{Al}_2\text{O}_3$ /SUS for catalytic  $\text{NH}_3$  oxidation

Catalyst (strip size)	Pt surface area <sup>a</sup> ( $\text{m}^2$ )	Surface Pt ( $\mu\text{mol}$ )	$\text{NH}_3$ conv. <sup>a</sup> (%)	Reaction rate ( $\mu\text{mol min}^{-1}$ )	TOF <sup>e</sup> ( $\text{min}^{-1}$ )
Pt/p-SUS ( $3 \times 10 \text{ mm}^2$ )	$3.0 \times 10^{-5}$	$7.67 \times 10^{-4}$ <sup>b</sup>	15.3	0.205	267
Pt/SUS ( $3 \times 30 \text{ mm}^2$ )	$9.1 \times 10^{-5}$	$2.33 \times 10^{-3}$ <sup>b</sup>	18.7	0.250	107
Pt/ $\text{Al}_2\text{O}_3$ /SUS ( $3 \times 30 \text{ mm}^2$ )	$14.4 \times 10^{-5}$	$3.69 \times 10^{-3}$ <sup>b</sup>	6.2	0.083	22
—	—	$1.12 \times 10^{-2}$ <sup>c</sup>	6.2	0.083	7

<sup>a</sup> Determined by a confocal laser scanning microscope. <sup>b</sup> Determined by the geometric area of the foil surface, surface coverage (100%), Sdr, and average surface atomic density of Pt ( $1.54 \times 10^{19}$  atom per  $\text{m}^2$ ). <sup>c</sup> Determined by the CO chemisorbed at  $50^\circ\text{C}$  assuming the stoichiometry of CO/Pt = 1. <sup>d</sup>  $\text{NH}_3$  conversion at  $200^\circ\text{C}$  (300 ppm  $\text{NH}_3$ , 8%  $\text{O}_2$ , 10%  $\text{H}_2\text{O}$ , and a He balance,  $100 \text{ mL min}^{-1}$ ). <sup>e</sup> Turnover frequency of the  $\text{NH}_3$  conversion at  $200^\circ\text{C}$ .

Table 2 Partial pressure dependences of  $\text{NH}_3$  oxidation

	Pt/p-SUS			Pt/SUS			Pt/ $\text{Al}_2\text{O}_3$ /SUS		
	$P_{\text{NH}_3}$ <sup>a</sup>	$P_{\text{O}_2}$ <sup>a</sup>	$P_{\text{H}_2\text{O}}$ <sup>a</sup>	$P_{\text{NH}_3}$ <sup>b</sup>	$P_{\text{O}_2}$ <sup>b</sup>	$P_{\text{H}_2\text{O}}$ <sup>b</sup>	$P_{\text{NH}_3}$ <sup>c</sup>	$P_{\text{O}_2}$ <sup>c</sup>	$P_{\text{H}_2\text{O}}$ <sup>c</sup>
Reaction order for $\text{NH}_3$ conversion rate	1.01	-0.35	-0.39	0.74	-0.30	-0.16	0.79	-0.67	-0.23

<sup>a</sup> Measured at 180 °C. <sup>b</sup> Measured at 190 °C. <sup>c</sup> Measured at 210 °C.

information about the reaction mechanism, partial orders concerning  $\text{NH}_3$ ,  $\text{O}_2$  and  $\text{H}_2\text{O}$  partial pressures for the conversion rates of  $\text{NH}_3$  were determined (Table 2 and Fig. S5†). Pt/p-SUS displayed a positive reaction order for  $\text{NH}_3$  (1.01) but negative orders for both  $\text{O}_2$  (-0.35) and  $\text{H}_2\text{O}$  (-0.39). This observation can be rationalised by assuming that the Pt surface site is predominantly occupied by adsorbed  $\text{O}_2$  and  $\text{H}_2\text{O}$  owing to their abundance in the gas phase. Similar outcomes were observed for unpolished Pt/SUS, although Pt/ $\text{Al}_2\text{O}_3$ /SUS exhibited a more negative order for  $\text{O}_2$  (-0.67). Consequently, the lower TOF over Pt/ $\text{Al}_2\text{O}_3$ /SUS could be attributed to the more dominant adsorption of  $\text{O}_2$  onto the surface Pt site. These partial orders are characteristic of the present reaction condition in an excess  $\text{O}_2$  and the result will be different under  $\text{NH}_3$ -rich conditions, where the Pt surface is primarily covered with nitrogen-containing species.

The Pt oxidation state of these samples was examined *via* XPS analysis (Fig. 6). Despite the surface roughness, the Pt 4d spectra showed that the fraction of metallic Pt was only slightly higher in Pt/p-SUS and Pt/SUS ( $\text{Pt}^0/\text{Pt} \sim 92\%$ ) compared to Pt/ $\text{Al}_2\text{O}_3$ /SUS ( $\text{Pt}^0/\text{Pt} < 90\%$ ). These fractions were kept almost unchanged even after use in the catalytic test at  $\leq 300$  °C. It is

widely acknowledged that metallic Pt is more active than oxidised Pt for the dissociation of adsorbed  $\text{O}_2$  molecules.<sup>13,39</sup> A more noticeable contrast was observed in the O 1s spectra; notably, the Pt/p-SUS sample exhibited a significantly lower O 1s peak than Pt/SUS and Pt/ $\text{Al}_2\text{O}_3$ /SUS. The peak was very broad in the range of binding energy 530–534 eV, and thus contained different components. Based on the literature assignment,<sup>40–45</sup> the peak could be partitioned into contributions from Pt oxide, adsorbed oxygen and  $\text{H}_2\text{O}$ , although the contribution from oxide was small because the Pt surface was mostly in a metallic state. Assuming this peak is attributed to adsorbed oxygen species,<sup>46,47</sup> this finding suggests that the stability of adsorbed oxygen on Pt/p-SUS is considerably lower than that on the other samples. Such situations may explain the smaller negative order in  $\text{O}_2$  for Pt/p-SUS relative to Pt/ $\text{Al}_2\text{O}_3$ /SUS (Table 2). Previous surface science studies have indicated that  $\text{NH}_3$  oxidation on Pt is initiated by forming reactive intermediate  $\text{NH}_x$  species through N–H bond cleavage, with atomic oxygen provided by adsorbed  $\text{O}_2$  playing a pivotal role.<sup>13,16,19,48</sup> The adsorbed oxygen is bound weakly on terrace sites but strongly on edge sites.<sup>32,49</sup> Furthermore, the nature of the adsorbed oxygen species may vary from atomic (on terrace

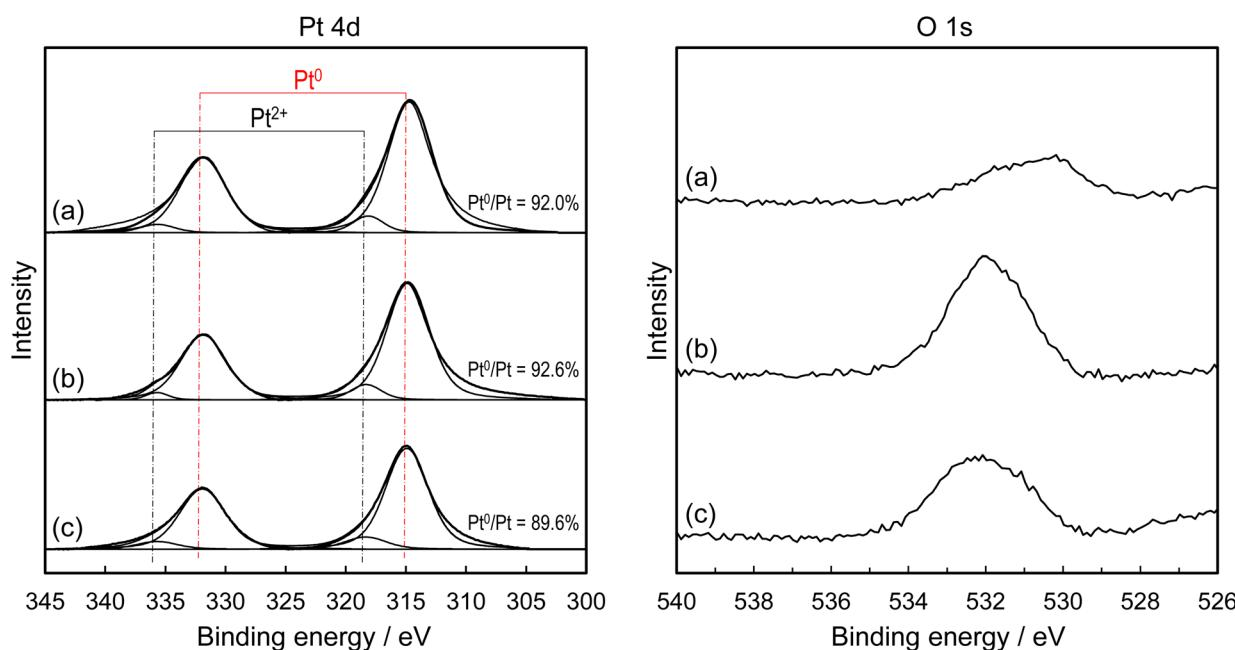


Fig. 6 Pt 4d and O 1s XPS spectra of (a) Pt/p-SUS, (b) Pt/SUS and (c) Pt/ $\text{Al}_2\text{O}_3$ /SUS (2000 shot AP pulses). The peak intensity is normalised by Pt 4f peaks because the Pt overlayer fully covered the surface of the metal foil catalysts.

sites) to ionic (on edge sites).<sup>50</sup> Based on the hypothesis and O 1s XPS results (Fig. 6), strongly bound oxygen species are believed to be less abundant on Pt/p-SUS than on Pt/Al<sub>2</sub>O<sub>3</sub>/SUS, thus affecting the catalytic activity. Considering that the Pt overlayer samples contain structural varieties (terraces, steps, kinks, and other defects), it seems difficult to discuss the reactivity of these different oxygen species toward NH<sub>3</sub>. Nonetheless, the present kinetic studies indicated that the NH<sub>3</sub> oxidation rate showed a more positive order in NH<sub>3</sub> pressure but showed a less negative order in O<sub>2</sub> pressure over Pt/p-SUS compared to Pt/Al<sub>2</sub>O<sub>3</sub>/SUS. The result implies that the nanometric smoothness of the Pt surface is favored for the facile adsorption and activation of NH<sub>3</sub> in excess oxygen. The surface reaction between NH<sub>x</sub> and atomic oxygen results in a higher concentration of nitrogen atoms, leading to the formation of N<sub>2</sub> through the combination of two adsorbed nitrogens. This provides a plausible explanation for the observed higher N<sub>2</sub> selectivity in Pt/p-SUS.

## 4. Conclusions

In this study, we utilised a pulsed cathodic arc–plasma deposition method to fabricate a nanometric Pt overlayer on 50 µm-thick SUS foil substrates featuring varying degrees of surface roughness, *i.e.*, p-SUS, SUS and Al<sub>2</sub>O<sub>3</sub>/SUS. We assessed the surface roughness quantitatively and qualitatively through comprehensive analysis employing SEM, STEM-EDS, laser scanning confocal microscopy and chemisorption techniques. Notably, the surface roughness ( $R_a$ ) exhibited a descending trend, with Pt/Al<sub>2</sub>O<sub>3</sub>/SUS (179 nm) demonstrating the highest value, followed by Pt/SUS (94 nm) and then Pt/p-SUS (8 nm). Consequently, the surface area ratio (Sdr) and the number of active sites declined correspondingly in this order. However, despite these trends, the NH<sub>3</sub> oxidation activity measured at 200 °C exhibited the opposite order. Specifically, the calculated TOF was most pronounced for Pt/p-SUS (267 min<sup>-1</sup>), followed by Pt/SUS (107 min<sup>-1</sup>) and Pt/Al<sub>2</sub>O<sub>3</sub>/SUS ( $\leq 22$  min<sup>-1</sup>). This unexpected result underscores the sensitivity of high-TOF NH<sub>3</sub> oxidation over Pt overlayer catalysts to their nanometric surface roughness. Moreover, we observed that the surface smoothness of the Pt overlayer conferred benefits in terms of yielding N<sub>2</sub> over an undesirable byproduct (N<sub>2</sub>O).

## Data availability

The data supporting this study's findings are available from the corresponding author upon reasonable request.

## Author contributions

M. Machida proposed, planned the research and wrote the manuscript. N. Yamasaki, T. Miyoshi and H. Kusaba performed the sample preparation and catalytic reactions, and analyzed the data under the supervision of

M. Machida. K. Awaya, H. Yoshida, J. Ohyama and T. Sato performed characterisation. T. Ohori, K. Oka, K. Fujii and N. Ishikawa performed electron microscopic characterisation. The manuscript was written with input from all authors, and all authors have approved the final version.

## Conflicts of interest

The authors declare no conflict of interest.

## Acknowledgements

This work was financially supported by JSPS KAKENHI (Grant Number 22H00277). The authors thank the Kanagawa Institute of Industrial Science and Technology for cooperation in the FIB and STEM experiments.

## References

- 1 S. Misumi, H. Yoshida, S. Hinokuma, T. Sato and M. Machida, *Sci. Rep.*, 2016, **6**, 29737.
- 2 H. Yoshida, K. Koizumi, M. Boero, M. Ehara, S. Misumi, A. Matsumoto, Y. Kuzuhara, T. Sato, J. Ohyama and M. Machida, *J. Phys. Chem. C*, 2019, **123**, 6080–6089.
- 3 H. Yoshida, S. Misumi, A. Matsumoto, Y. Kuzuhara, T. Sato, J. Ohyama and M. Machida, *Catal. Sci. Technol.*, 2019, **9**, 2111–2117.
- 4 M. Machida, Y. Tokudome, A. Maeda, Y. Kuzuhara, T. Hirakawa, T. Sato, H. Yoshida, J. Ohyama, K. Fujii and N. Ishikawa, *ACS Catal.*, 2020, **10**, 4677–4685.
- 5 M. Machida, Y. Tokudome, A. Maeda, T. Koide, T. Hirakawa, T. Sato, M. Tsushida, H. Yoshida, J. Ohyama, K. Fujii and N. Ishikawa, *ACS Omega*, 2020, **5**, 32814–32822.
- 6 M. Machida, Y. Tokudome, A. Maeda, T. Sato, H. Yoshida, J. Ohyama, K. Fujii and N. Ishikawa, *Catal. Today*, 2022, **384–386**, 70–75.
- 7 H. Yoshida and M. Machida, *ChemCatChem*, 2023, **15**, e202300771.
- 8 M. Machida and H. Yoshida, *Mater. Trans. JIM*, 2023, **64**, 2369–2375.
- 9 J. Zhou, B. Guan, J. Guo, C. Zheng, T. Su, J. Chen, Y. Zhang, Y. Yuan, H. Dang, Y. He, Z. Wei, B. Xu, C. Xu, C. Yi, W. Zeng and Z. Huang, *Ind. Eng. Chem. Res.*, 2023, **62**, 20506–20546.
- 10 T. Lan, Y. Zhao, J. Deng, J. Zhang, L. Shi and D. Zhang, *Catal. Sci. Technol.*, 2020, **10**, 5792–5810.
- 11 L. Chmielarz and M. Jabłońska, *RSC Adv.*, 2015, **5**, 43408–43431.
- 12 F. Gao, Y. Liu, Z. Sani, X. Tang, H. Yi, S. Zhao, Q. Yu and Y. Zhou, *J. Environ. Chem. Eng.*, 2021, **9**, 104575.
- 13 W. D. Mieher and W. Ho, *Surf. Sci.*, 1995, **322**, 151–167.
- 14 Y. Li and J. N. Armor, *Appl. Catal., B*, 1997, **13**, 131–139.
- 15 A. C. M. van den Broek, J. van Grondelle and R. A. van Santen, *J. Catal.*, 1999, **185**, 297–306.

16 J. Pérez-Ramírez, E. V. Kondratenko, V. A. Kondratenko and M. Baerns, *J. Catal.*, 2004, **227**, 90–100.

17 C. J. Weststrate, J. W. Bakker, A. C. Gluhoi, W. Ludwig and B. E. Nieuwenhuys, *Catal. Today*, 2010, **154**, 46–52.

18 S. Hinokuma, H. Shimano, S. Matsuki, M. Kawano, Y. Kawabata and M. Machida, *Chem. Lett.*, 2016, **45**, 179–181.

19 H. Ma and W. F. Schneider, *ACS Catal.*, 2019, **9**, 2407–2414.

20 D. A. Svintsitskiy, L. S. Kibis, A. I. Stadnichenko, E. M. Slavinskaya, A. V. Romanenko, E. A. Fedorova, O. A. Stonkus, D. E. Doronkin, V. Marchuk, A. Zimina, M. Casapu, J.-D. Grunwaldt and A. I. Boronin, *ChemCatChem*, 2020, **12**, 867–880.

21 E. M. Slavinskaya, L. S. Kibis, O. A. Stonkus, D. A. Svintsitskiy, A. I. Stadnichenko, E. A. Fedorova, A. V. Romanenko, V. Marchuk, D. E. Doronkin and A. I. Boronin, *ChemCatChem*, 2021, **13**, 313–327.

22 C. Fukuhara, R. Hyodo, K. Yamamoto, K. Masuda and R. Watanabe, *Appl. Catal., A*, 2013, **468**, 18–25.

23 C. Xu, X. Zhang and Z. Yang, *J. Phys.: Condens. Matter*, 2020, **32**, 175201.

24 K. Hayashi, S. Kameoka and A.-P. Tsai, *Mater. Trans. JIM*, 2021, **62**, 1089–1096.

25 R. A. Van Santen, *Acc. Chem. Res.*, 2009, **42**, 57–66.

26 C. H. F. Peden, D. N. Belton and S. J. Schmieg, *J. Catal.*, 1995, **155**, 204–218.

27 G. C. Bond, *Acc. Chem. Res.*, 1993, **26**, 490–495.

28 Y. F. Zeng and R. Imbihl, *J. Catal.*, 2009, **261**, 129–136.

29 K. Yang and B. Yang, *Appl. Surf. Sci.*, 2022, **584**, 152584.

30 J. L. Gland and V. N. Korchak, *J. Catal.*, 1978, **53**, 9–23.

31 E. Xue, K. Seshan and J. R. H. Ross, *Appl. Catal., B*, 1996, **11**, 65–79.

32 L. M. Carballo and E. E. Wolf, *J. Catal.*, 1978, **53**, 366–373.

33 M. C. Demicheli, L. C. Hoang, J. C. Ménézo, J. Barbier and M. Pinabiau-Carlier, *Appl. Catal., A*, 1993, **97**, L11–L17.

34 T. F. Garetto and C. R. Apesteguía, *Appl. Catal., B*, 2001, **32**, 83–94.

35 T. F. Garetto and C. R. Apesteguía, *Catal. Today*, 2000, **62**, 189–199.

36 H. Lieske, G. Lietz, H. Spindler and J. Völter, *J. Catal.*, 1983, **81**, 8–16.

37 A. Borgna, F. Le Normand, T. Garetto, C. R. Apesteguía and B. Moraweck, *Catal. Lett.*, 1992, **13**, 175–188.

38 R. M. Heck, R. J. Farrauto and S. T. Gulati, *Catalytic Air Pollution Control: Commercial Technology*, Wiley, Hoboken, 1995.

39 D. P. Sobczyk, E. J. M. Hensen, A. M. de Jong and R. A. van Santen, *Top. Catal.*, 2003, **23**, 109–117.

40 N. Materer, U. Starke, A. Barbieri, R. Döll, K. Heinz, M. A. Van Hove and G. A. Somorjai, *Surf. Sci.*, 1995, **325**, 207–222.

41 J. F. Zhu, M. Kinne, T. Fuhrmann, B. Tränkenschuh, R. Denecke and H. P. Steinrück, *Surf. Sci.*, 2003, **547**, 410–420.

42 A. C. Luntz, J. Grimblot and D. E. Fowler, *Phys. Rev. B: Condens. Matter Mater. Phys.*, 1989, **39**, 12903–12906.

43 C. Puglia, A. Nilsson, B. Hernnäs, O. Karis, P. Bennich and N. Mårtensson, *Surf. Sci.*, 1995, **342**, 119–133.

44 M. Peuckert and H. P. Bonzel, *Surf. Sci.*, 1984, **145**, 239–259.

45 W. Ranke and H. J. Kuhr, *Phys. Rev. B: Condens. Matter Mater. Phys.*, 1989, **39**, 1595–1601.

46 C. J. Weststrate, J. W. Bakker, E. D. L. Rienks, C. P. Vinod, A. V. Matveev, V. V. Gorodetskii and B. E. Nieuwenhuys, *J. Catal.*, 2006, **242**, 184–194.

47 J. L. G. Fierro, J. M. Palacios and F. Tomas, *Surf. Interface Anal.*, 1988, **13**, 25–32.

48 G. Novell-Leruth, J. M. Ricart and J. Pérez-Ramírez, *J. Phys. Chem. C*, 2008, **112**, 13554–13562.

49 H. Wang, R. G. Tobin, D. K. Lambert, C. L. DiMaggio and G. B. Fisher, *Surf. Sci.*, 1997, **372**, 267–278.

50 A. R. Vaccaro, G. Mul, J. Pérez-Ramírez and J. A. Moulijn, *Appl. Catal., B*, 2003, **46**, 687–702.